JGR Solid Earth

RESEARCH ARTICLE
10.1029/2019JB018203

Melt Segregation and Depletion During Ascent of Buoyant Diapirs in Subduction Zones

Nan Zhang[1,2,3], Mark D. Behn[1,4], E. Marc Parmentier[5], and Christopher Kincaid[6]

[1]Department of Geology and Geophysics, Woods Hole Oceanography Institution, Woods Hole, MA, USA, [2]Key Laboratory of Orogenic Belts and Crustal Evolution, School of Earth and Space Sciences, Peking University, Beijing, China, [3]Earth Dynamics Research Group, Department of Applied Geology, Curtin University, Perth, Western Australia, Australia, [4]Department of Earth and Environmental Sciences, Boston College, Chestnut Hill, MA, USA, [5]Department of Earth, Environmental and Planetary Sciences, Brown University, Providence, RI, USA, [6]School of Oceanography, University of Rhode Island, Narragansett, RI, USA

Abstract Cold, low-density diapirs arising from hydrated mantle and/or subducted sediments on the top of subducting slabs have been invoked to transport key chemical signatures to the source region of arc magmas. However, to date there have been few quantitative models to constrain melting in such diapirs. Here we use a two-phase Darcy-Stokes-energy model to investigate thermal evolution, melting, and depletion in a buoyant sediment diapir ascending through the mantle wedge. Using a simplified 2-D circular geometry, we investigate diapir evolution in three scenarios with increasing complexity. In the first two scenarios we consider instantaneous heating of a diapir by thermal diffusion with and without the effect of the latent heat of melting. Then, these simplified calculations are compared to numerical simulations that include melting, melt segregation, and the influence of depletion on the sediment solidus along pressure-temperature-time (*P-T-t*) paths appropriate for ascent through the mantle wedge. The high boundary temperature induces a rim of high porosity, into which new melts are focused and then migrate upward. The rim thus acts like an annulus melt channel, while the effect of depletion buffers additional melt production. Solid matrix flow combined with recrystallization of melt pooled near the top of the diapir can result in large gradients in depletion across the diapir. These large depletion gradients can either be preserved if the diapir leaks melt during ascent, or rehomogenized in a sealed diapir. Overall our numerical simulations predict less melt production than the simplified thermal diffusion calculations. Specifically, we show that diapirs whose ascent paths favor melting beneath the volcanic arc will undergo no more than ~40–50% total melting.

Key Points:
- This study explores thermal and chemical evolution of diapirs rising through the mantle wedge
- We use a two-phase Darcy-Stokes-energy model to investigate thermal evolution, melting, and melt segregation in such a diapir
- Melt migration in ascending diapir segregates interior from outer rim; segregation may be preserved, if the diapir leaks melt during ascent

Supporting Information:
- Supporting Information S1
- Data Set S1
- Data Set S2
- Data Set S3
- Data Set S4
- Data Set S5
- Data Set S6

Correspondence to:
N. Zhang,
nan_zhang@pku.edu.cn

Citation:
Zhang, N., Behn, M. D., Parmentier, E. M., & Kincaid, C. (2020). Melt segregation and depletion during ascent of buoyant diapirs in subduction zones. *Journal of Geophysical Research: Solid Earth*, *125*, e2019JB018203. https://doi.org/10.1029/2019JB018203

Received 17 JUN 2019
Accepted 29 JAN 2020
Accepted article online 31 JAN 2020

1. Introduction

As early as the 1970s, Marsh and Carmichael (1974) suggested that the spacing of arc volcanoes was related to the development of gravitational instabilities formed from a thin "ribbon" of buoyant melt pooled along the surface of the subducting slab. More recently, Hall and Kincaid (2001) invoked the rapid ascent of melt diapirs to explain U-series disequilibrium observed in many arc lavas (e.g., Ivanovich & Harmon, 1982). Other sources of buoyancy have also been proposed to drive diapirism from the descending slab. Gerya and Yuen (2003) proposed the development of "cold plumes" that originate from a layer of buoyant hydrated mantle lying just above the downgoing slab. Numerical models suggest that such cold plumes can be up to tens of kilometers in diameter, entrain significant amounts of sediment/crustal material from the slab, and dramatically influence the thermal and chemical dynamics of the mantle wedge (Castro & Gerya, 2008; Gerya & Yuen, 2003; Gorczyk et al., 2006; Marschall & Schumacher, 2012; Nielsen & Marschall, 2017; Zhu et al., 2009). Others have argued that subducted sediments may be the primary source of buoyancy, invoking a model in which sediment diapirs rise and melt as they ascend through the mantle wedge (Behn et al., 2011; Currie et al., 2007; Kelemen et al., 2003, 2003; Miller & Behn, 2012; Spencer et al., 2017). Diapiric ascent from a sedimentary layer has been used to explain both the ubiquitous presence of a "sediment signature" (enrichment in fluid-immobile elements such as Ba, Th, Be, Pb, and other light rare earth elements) in arc lavas (e.g., Elliott et al., 1997; Hawkesworth et al., 1997; Plank & Langmuir, 1993), as well as geochemical constraints that indicate this melting occurs dominantly in the mantle wedge as opposed to on the slab surface (Behn et al., 2011). However, while there is accumulating evidence that diapirs play an important role in subduction zone dynamics (Cruz-Uribe et al., 2018; Liu et al., 2015; Marschall

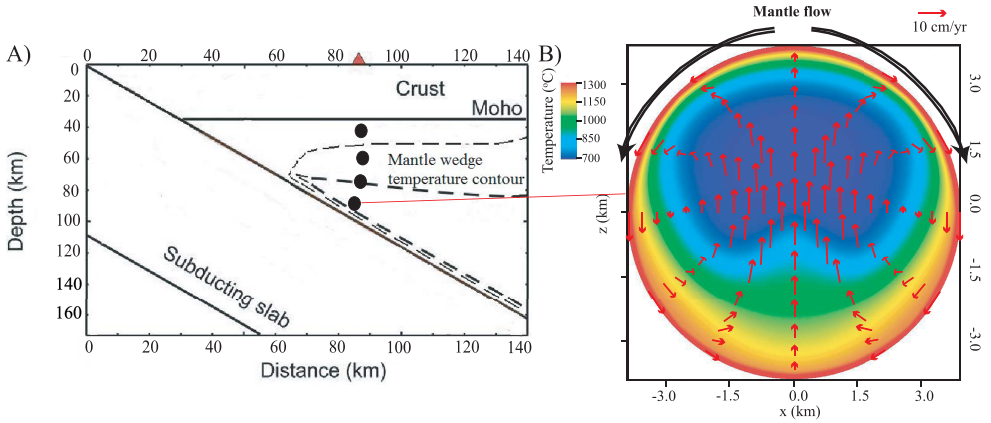

Figure 1. (a) Schematic showing the ascent of a sediment diapir through the mantle wedge and (b) solid velocity field inside an ascending diapir associated with the Stokes flow on the margins. A 3.5-km radius diapir with a density of 3,000 kg/m^3 is calculated to move upward at a velocity of 10 cm/year assuming a mantle wedge viscosity of 5×10^{18} Pa·s. Here the velocity field is used to calculate a representative internal temperature field assuming no melting.

& Schumacher, 2012; Nielsen & Marschall, 2017), there have been few quantitative modeling studies that investigate both the solid advection of buoyant material, as well as the physical process of melting, melt segregation, and depletion in these environments. Such models are necessary to better understand the depletion of ultrahigh-pressure rocks that record the residues of this melting process (Hacker et al., 2005) and the relationship between melt segregation and the observed "sediment signature" in arc lavas.

Here we focus on the physical processes of thermal evolution, melting, and melt segregation within the end-member of an ascending sediment diapir, acknowledging that the composition of diapirs in natural settings may involve more complex mixtures of sediment and hydrated crustal and mantle rocks. As a buoyant diapir rises from the cold slab top through the hot mantle wedge, the surrounding mantle will heat the diapir, promoting melting along its boundary (e.g., Ghods & Arkani-Hamed, 2002). Melt generated at the boundary will in turn segregate and migrate within this deforming matrix. The resulting melt-matrix interaction plays a key role in fractionating volatile and incompatible elements within the diapir and in turn influences its chemical evolution of the depleted residuum.

Melt migration in ascending mantle plumes has been investigated in previous studies. Ghods and Arkani-Hamed (2002) and Schmeling (2000) studied melt migration in hot plumes rising through the upper mantle. These studies modeled a plume in a continuous compacting porous media, in which the plume is driven by thermal buoyancy and deforms along its path toward the surface. Both studies found a region of high melt fraction concentrated at the top of the plume, and that the high melt fraction region ascends faster than the bulk of the plume. However, neither of these studies investigated the dynamics of a fertile, compositionally buoyant diapir that is chemically distinct from the surrounding mantle. In the closest related study, Katz and Rudge (2011) investigated energy conservation in a fertile heterogeneity ascending through the mantle and estimated the evolution of the average melt fraction within the heterogeneity. Their model predicts that thermal diffusion into a spherical heterogeneity can produce >50% melt for bodies with diameters smaller than ~1 km. However, Katz and Rudge (2011) did not explore the migration and segregation of these melts or the depletion of the residue during diapir ascent.

In this study, we investigate melt generation and migration in a cold, fertile sediment diapir (Figure 1) rising from a subducting slab and heating and convecting during ascent through the mantle wedge. Diapir geometry is simplified as a two-dimensional (2-D) circle and pressure-temperature-time (*P-T-t*) ascent paths are estimated from subduction zone thermal models. Two-phase flow simulations are used to calculate melting and depletion within the diapir. We find that melts preferentially migrate upward within an annulus channel at the margins of the diapir where conductive heating generates a melt-rich, high permeability layer. Depletion of the margins buffers additional melt production and promotes the creation of strong chemical gradients within the diapir, with a highly depleted (and more refractory) rim surrounding a less depleted and more primitive interior.

2. Model Description and Methods

2.1. Model and Mathematical Formulation

We use a numerical model to investigate the internal structure of an ascending diapir as it rises through the mantle wedge of a subduction zone. The internal melt-solid two-phase flow is calculated assuming a fixed diapir morphology, in which the diapir head is simplified as a 2-D circle. This simplification is reasonable based on previous laboratory and numerical experiments (Hall & Kincaid, 2001; Marsh, 1979; Miller & Behn, 2012), which show little deformation of the diapir head during ascent. This 2-D circle can be easily implemented with the software package we use (see section 2.5). Using this 2-D circular geometry, we model two-phase flow of the melt and matrix along pressure-temperature-time (P-T-t) trajectories appropriate for ascent of a diapir through an idealized mantle wedge. Limitations of our simplified geometry and avenues for future research are discussed in section 4.2.

2.2. Two-Phase Flow

Our treatment of two-phase melt migration is based on McKenzie (1984) and the subsequent reanalysis by Spiegelman et al. (2007). Mass conservation for the melt and total solid take the form

$$\frac{\partial \phi}{\partial t} + \nabla\cdot\left(\phi\vec{v}\right) = \dot{\Gamma} \tag{1}$$

$$\frac{\partial (1-\phi)}{\partial t} + \nabla\cdot\left((1-\phi)\vec{W}\right) = -\dot{\Gamma} \tag{2}$$

where ϕ is the porosity, t is the time, $\vec{v}$ and $\vec{W}$ are the melt and solid velocities, respectively, and $\dot{\Gamma}$ is the melting/crystallization rate. These mass conservation formulations neglect the change in melt density during melting (McKenzie, 1984). The force balance for melt follows Darcy's law

$$\vec{S} = \phi\left(\vec{v}-\vec{W}\right) = -\frac{K}{\mu}\left(\nabla P - \Delta\rho g\vec{e_z}\right) \tag{3}$$

where $\vec{S}$ is the Darcy flux, K is the permeability, μ is the melt viscosity, P is the effective pressure (Phipps, 1987), $\Delta\rho = \rho_s - \rho_f$ is the density difference between the solid and the melt, g is the gravitational acceleration, and $\vec{e_z}$ is the unit vector (positive upward). Permeability depends on porosity through a power law relation (von Bargen & Waff, 1986; Wark & Watson, 1998):

$$K = \frac{d^2}{C}\phi^n \tag{4}$$

where d is grain size and C is a geometrical factor. The exponent n takes on values of 1–3 (Riley & Kohlstedt, 1991; Wark et al., 2003; Wark & Watson, 1998; Zhu & Hirth, 2003). Following recent experimental studies (Miller et al., 2014), we choose $n = 3$ for the simulations shown in this study. A constant grain size of 1 cm is used in all simulations based on the average value for the mantle wedge from Wada et al. (2011).

Similar to Scott and Stevenson (1986), we approximate the difference between the melt and the solid pressures by compaction rate of the matrix ($\nabla\cdot\vec{W}$) times bulk viscosity ξ (McKenzie, 1984),

$$P_c = P_f - P_s = \xi\nabla\cdot\vec{W}, \tag{5}$$

where

$$\xi = \frac{\eta}{\phi} \tag{6}$$

and η is the shear viscosity of the solid, which is assumed to be constant in our calculations.

This implies that differences between the solid and fluid pressure drive volume changes of the solid matrix, for example, the matrix will expand if the fluid pressure exceeds the solid pressure ($P_f > P_s$). This formulation is consistent with the derivation of Scott and Stevenson (1984, 1986). In the simulations considered here, we assume that the shear viscosity (Hirth & Kohlstedt, 2004) of the mantle wedge is constant.

Table 1
Model Parameters

Parameters	Value
The thickness of sediment layer on slab, h	1.1–0.2 km
Melt density, ρ_f	2,300 kg/m^3
Solid sediment density, ρ_s	2,800 kg/m^3(2,700–3,000 kg/m^3)
Maximum mantle wedge temperature, T_M	1300 °C
Reference temperature of slab, T_0	700 °C
Thermal diffusivity, κ	10^{-6} m^2/s
Shear viscosity of solid matrix, η_0	1×10^{18}, 5×10^{18}, 5×10^{19}Pa·s
Melt viscosity, μ	1 Pa·s
Gravitational acceleration, g	9.81 m/s^2
Thermal expansion, α	10^{-4} K^{-1}
Temperature difference, ΔT	600 K
Latent heat, L	3.5×10^5 J/kg
Grain size, d	1 cm
Mantle wedge density, ρ_m	3,400 kg/m^3
Reference permeability, K_0	3.3×10^{-13} m
Compaction length, δ_c	5.7, 12.8, 40.5 km
Mantle specific heat, c_p	1250 J·kg^{-1}·K^{-1}
Grain geometry constant, C	300 (Wark &Watson, 1998)
Reaction rate, Re	≥1/100 yr^{-1}
Threshold pressure of dike, p_{dike}	10 MPa (Havlin et al., 2013)
Mantle wedge viscosity, η_m	5×10^{18} Pa·s

The effective pressure can be obtained by solving a Helmholtz equation obtained by combining equations ((1)) and ((2)), and the divergence of equation ((3)),

$$\nabla\cdot\left[\frac{K}{\mu}\left(\nabla P-\Delta\rho g\vec{e_z}\right)\right]=\frac{P-p_r}{\xi} \tag{7}$$

where p_r is the pressure induced by the rotational flow (Stokes-Hadamard solution; Batchelor, 1967). For the simplified circular diapir considered here, its internal solid flow can be decomposed to a rotational flow and an irrotational flow (compaction flow) (e.g., Spiegelman, 1993),

$$\vec{W}=\vec{W}^r+\vec{W}^c=\nabla\times\vec{\Omega}+\nabla\Psi \tag{8}$$

where $\vec{W}^r$ is the rotational flow and $\vec{W}^c$ is the compaction flow. $\vec{\Omega}$ is the vector potential, and Ψ is the scalar potential. For the case of the diapirs considered here, the magnitude of rotational flow induced by shear on the margins of the ascending sphere will be significantly greater than the internal flow induced by the ambient corner flow in the mantle wedge (see section 2.4 below). Thus, we assume that internal Stokes solid flow in the diapir is driven solely by ascending sphere induced rotational flow. This rotational flow in a spherical diapir of constant viscosity can be obtained through the analytic solution [Stokes-Hadamard solution; Batchelor, 1967], although our model uses a circular geometry (we return this issue in Discussion Section). This assumed rotational flow also induces a constant pressure gradient field [Stokes-Hadamard solution; Batchelor, 1967], which is included in our pressure term P.For the solid compaction flow, we substitute equation (8) into (5) to get

$$\nabla^2\Psi=\frac{P-p_r}{\xi} \tag{9}$$

Combining the equations (9), (7), and (3), we have solutions for pressure and velocities of solid and melt. Melt generation consumes thermal energy through latent heat. The energy equation can thus be written as

$$\frac{\partial T}{\partial t}=\nabla\cdot\kappa\nabla T-\left(\phi\vec{v}+(1-\phi)\vec{W}\right)\cdot\nabla T-\frac{L\dot{\Gamma}}{c_p} \tag{10}$$

where T is temperature, L is the latent heat of melting, and $\rho=\rho_s\approx\rho_f$. The role of adiabatic heating is estimated to be small (see section 4.1) and is therefore assumed to be negligible. The viscous heating is also negligible because the solid rotational flow only produces a small heat, and the compaction deformation is comparable to the rotational deformation. The melting rate $\dot{\Gamma}$ is determined by the difference between the equilibrium melt fraction and the melt present in any infinitesimal parcel (Dannberg & Heister, 2016; Katz, & Weatherley, 2012; Keller & Katz, 2016).

$$\dot{\Gamma}=Re(\phi^{eq}-\phi) \tag{11}$$

where Re is the reaction rate (Table 1; Keller & Katz, 2016), and the equilibrium melt fraction φ^{eq} is scaled by the temperature difference between the liquidus (T_L) and the solidus (T_S)

$$\phi^{eq}=\frac{T-T_S}{T_L-T_S}\ \text{ with } TS=T_{S0}(p)+\Delta T_F F \tag{12}$$

where $T_{S0}(p)$ is the sediment solidus without depletion, F is the degree of melting (depletion), and ΔT_F represents the effect of depletion on the solidus (Figure 2). ϕ^{eq} is set to 0 when the temperature is below solidus. The pressure-dependent solidus $T_{S0}(p)$ is derived from the water-saturated and anhydrous sediment solidi of Schmidt (2015) and Mann and Schmidt (2015), respectively. Our solidus for zero depletion is an average of

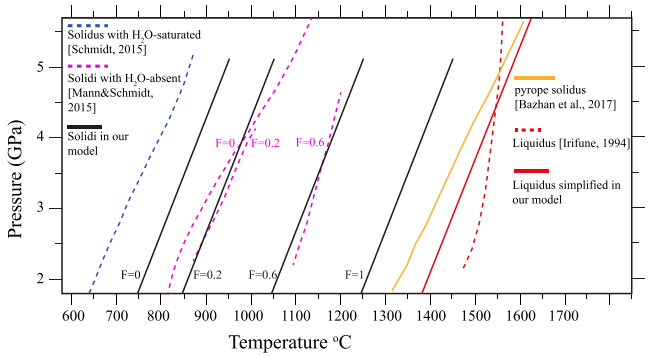

Figure 2. Parameterizations of sediment solidus (solid black curves) and liquidus (solid red curve) used in this study. The sediment solidus is assumed to vary with the total amount of depletion (F). Experimentally determined solidi for H_2O-saturated (dark blue) and H_2O-absent (pink) sediment melting are taken from Schmidt (2015) and Mann and Schmidt (2015), respectively. Experimental sediment liquidus (dashed red) from Irifune et al. (1994) is also shown. The solidus of pyrope is also plotted (yellow). Our model sediment solidus at $F = 0$ assumes a general average of the H_2O-saturated and H_2O-absent melting experiments.

these two and implies a solidus temperature of 820 °C at 3 GPa (Figure 2). The slope of the solidus with pressure is 80 K/GPa, which is smaller than that of the peridotite (Hirschmann, 2001; Katz, 2003). This solidus is similar to the H_2O fluid-absent solidus of Mann and Schmidt (2015) and is appropriate for melting in a rising diapir composed of hydrated sediments that are not fluxed with H_2O from below (Schmidt, 2015). The sediment liquidus is based on Irifune et al. (1994), who found that the sediment liquidus is ~550–650 K higher than the solidus in the upper mantle. In our models, the slopes of solidus and liquidus are assumed to be equal and the difference between the solidus and liquidus ($T_L - T_S$) at zero depletion is assumed to be 630 K (e.g., Dannberg & Heister, 2016). Further, to avoid the situation where ϕ^{eq} goes to infinity at $F = 1$, we set T_L to be slightly greater than T_S at $F = 1$. We note that this melting parameterization does not account the evolving composition of melt.

The additional term ΔT_F in equation (12) is important for determining the influence of depletion on melt generation. Typically, values of ΔT_F for peridotite melting are on order of ~200 K (Katz, 2003; see also equation (38) in Dannberg & Heister, 2016); however, the F-dependent melting of sediment is less well constrained. Mann and Schmidt (2015) showed that for 20% and 60% depletion the H_2O fluid absent sediment solidus is ~50 K to ~280 K higher, respectively, than the undepleted solidus (pink dashed curves in Figure 2). Further, we assume the final residue of sediment melting can be approximated as a pyrope-bearing granulite. The pyrope solidus (Bazhan et al., 2017) is ~550 K higher than that of sediment solidus for zero depletion (orange curves in Figure 2). Without additional constraints, we make the simplifying assumption that the role of depletion is linear and estimate the ΔT_F term in equation (12) to be 500 K. The black curves in Figure 2 show our parameterized depletion-dependent solidus. We note that while the amount of melt produced in our simulations is sensitive to our choice of ΔT_F, the underlying dynamics of melting and melt segregation within an ascending diapir is not strongly sensitive to this choice.

Another important term in our melting parameterization is the reaction rate Re. Currently, Re is not constrained for sediment melting. The peridotite reaction rate is regularly taken as 1/100 yr (Keller & Katz, 2016), and we employ that value in our models. We have also performed simulations with a reaction rate of 1/50 yr, and find that our model results are not strongly sensitive to these larger reaction rates.

Finally, we solve F (depletion) using

$$\frac{\partial F}{\partial t} + \vec{W}\cdot\nabla F = \dot{\Gamma} \tag{13}$$

Summarizing the system of equations described above, the five basic unknowns for our problem are ϕ, p, Ψ, T, and F. We solve for these variables using equations (1), (7), (9), (10), and (13) for melt migration, solid compaction, and the evolution of porosity, temperature, and depletion within the diapir.

2.3. Nondimensionalization, Scaling, and Parameters

It is convenient to recast the governing equations in nondimensional form for numerical implementation. We use the compaction length δ_c as our basic length scale (Schiemenz et al., 2011), which is the characteristic length over which compaction occurs

$$\delta_c = \sqrt{\frac{K_0\xi_0}{\mu}} \tag{14}$$

The other nondimensional scales are

$\vec{x} = \delta_c\vec{x}', P = p_0P', \phi = \phi_0\phi', \vec{W} = W_0\vec{W}', T = T_0+\Delta TT', \Psi = \Psi_0\Psi' = W_0\delta\Psi'$, where $\vec{x}$ is the coordinate, ϕ_0 is the reference porosity, which is set to 0.01 in this study, T_0 is the slab temperature, and ΔT is the temperature

difference between the slab temperature and the highest temperature in the mantle wedge T_M. The magnitude of ϕ_0 is chosen such that the initial porosity is close to 1. The scales for permeability, compaction viscosity, pressure, solid velocity, fluid velocity, and time are given as

$$K_0 = \frac{d^2}{C}{\phi_0}^3,\ \xi_0 = \frac{\eta}{\phi_0},\ p_0 = \frac{W_0\xi_0}{\delta_c},\ W_0 = \frac{K_0\Delta\rho g}{\mu},\ v_0 = \frac{W_0}{\phi_0},\ t_0 = \frac{\delta_c}{v_0}$$

Substituting the nondimensional variables into equations (1), (3), (7), (9), and (10), and dropping the prime notation, we arrive at the dimensionless governing equations (except equation (19), which is kept dimensional):

$$\nabla\cdot\left(\phi^3\nabla P\right) - P\phi = \frac{\partial\phi^3}{\partial z} - \phi p_r \tag{15}$$

$$\nabla^2\Psi = \phi(P - p_r) \tag{16}$$

$$\vec{v} = \phi_0\vec{W} - \frac{K}{\phi}\left(\nabla P - \vec{e_z}\right) \tag{17}$$

$$\frac{\partial\phi}{\partial t} + \nabla\cdot\left(\phi\vec{v}\right) = \frac{\delta}{v_0\phi_0}\dot{\Gamma} \tag{18}$$

$$\frac{\partial T}{\partial t} = \nabla\cdot\kappa\nabla T - \left(\phi\vec{v} + (1-\phi)\vec{W}\right)\cdot\nabla T - \frac{L\dot{\Gamma}}{c_p} \tag{19}$$

For the majority of our calculations we set the top of the diapir to be an impermeable boundary. Although the momentum equations (equations (1) and (2)) are valid only when melt flows within a continuous permeable solid matrix (Hier-Majumder et al., 2006; McKenzie, 1984; Schmeling et al., 2019; Zhu et al., 2011), we allow the porosity to exceed the disaggregation threshold (typically ~20–40%), but never increase above 100%. This treatment allows us to explore the total melt fraction in the system (e.g., Katz & Weatherley, 2012).

2.4. Diapir Pressure-Temperature-Time (*P-T-t*) Paths Through the Mantle Wedge

To define the boundary conditions on our two-phase flow calculations, a specified pressure-temperature-time (*P-T-t*) history appropriate for ascent through mantle wedge is imposed on the outer boundary of the diapir. The diapir trajectory is calculated based on a combination of Stokes flow (Batchelor, 1967) and the background wedge corner flow (McKenzie, 1969) (see supporting information). The rate of diapir ascent is estimated based on Stokes flow assuming the size and density of the diapir and the viscosity of the mantle wedge (e.g., Behn et al., 2007). The diameter of the diapir is determined from the size and spacing of the Rayleigh-Taylor instabilities that form from a buoyant sediment layer sitting atop a subducting slab. Previous modeling studies indicated that >90% of the buoyant material is entrained during instability formation (e.g., Miller & Behn, 2012). Thus, the primary controls on diapir size are the thickness of the sediment layer and the spacing of the instabilities.

Behn et al. (2011) calculated that for typical sediment layer thicknesses of 0.2–1.1 km (e.g., Clift & Vannucchi, 2004; von Huene & Scholl, 1991) diapirs will initiate at slab depths of 65–150 km, with thicker layers going unstable at shallower depths. Following Jull and Kelemen (1999), the fastest growing wave length for instability growth can be calculated as $\lambda = \frac{2\pi h}{k}$, where λ is wavelength, h is the sediment layer thickness, and k is the nondimensional wave number. For non-Newtonian temperature-dependent rheology, k can be determined numerically and is ~0.5 for sediment layers (e.g., Miller & Behn, 2012). For the expected range of sediment thicknesses (0.2–1.1 km), this results in wavelengths of 2.5 to 13.8 km. Assuming the instability is sourced from a square region of width λ and height h, the radius R of a circular diapir can be calculated as $\sqrt[3]{\frac{\lambda\times\lambda\times h}{\frac{4}{3}\pi}}$. For the expected sediment layer thicknesses and instability wavelengths, R is estimated to be ~0.67–3.7 km. For a ~3.5-km diapir ascending at ~10 cm/yr, the corresponding rotational flow creates an overturning circulation inside the diapir that takes ~400 kyr to complete one overturn (Figure 1) [see also Schmeling et al., 1988].

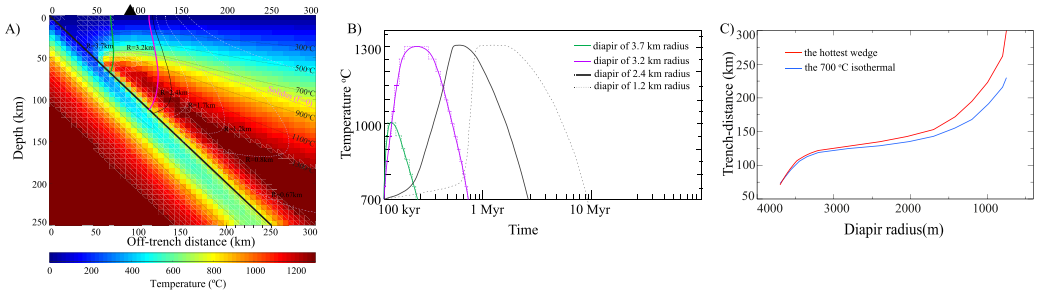

Figure 3. (a) Calculated sediment diapir trajectories superimposed on the mantle wedge thermal structures. (b) Calculated temperature evolution paths along the trajectories corresponding to diapir radii from 1.2 to 3.7 km. (c) Distance from the trench that a diapir will pass through the hottest portion of the mantle wedge (red) and intersect the 700 °C isotherm at the top of the wedge (blue) as a function of diapir radius. Wedge thermal structure is based on van Keken et al. (2008). The diapir radii are derived from instability analyses for different sediment thicknesses (Miller & Behn, 2012) and converted to radii as described in the text. The trajectories are calculated assuming the superposition of Stokes and isoviscous corner flow. Curves in (a) show trajectories for diapir radii ranging from 3.7 km (initialized at depth of 65 km) to 0.67 km (initialized at 150 km). The temperature-time (*T-t*) paths in (b) are extracted for four diapirs of radii 3.7, 3.2, 2.4, and 1.2 km.

Diapir *P-T-t* trajectories were then calculated based on the superposition of Stokes flow and mantle wedge corner flow. The Stokes velocity of the rising diapir was calculated

$$U_{Stokes} = \frac{1}{3}\frac{\rho_m - \rho_{diapir}}{\eta_m} g R^2 \tag{20}$$

where ρ_m is the mantle wedge density, ρ_{diapir} is the sediment density, η_m is the mantle wedge viscosity, and g is the gravitational acceleration (see Table 1 for parameter values). For the diapir radii estimated above, this gives a range of vertical ascent rates of 0.6–16.9 cm/yr, with the faster ascent rates corresponding to larger diapirs. The component of wedge corner flow $\vec{U}_C$ is estimated based on the analytical solution for an isoviscous mantle wedge (McKenzie, 1969) and assuming the diapir is sufficiently small that it does not disturb the overall corner flow pattern. To calculate $\vec{U}_C$ we assume a subduction dip angle of 45°, and subduction rate of 6 cm/yr; average values from Pacific subduction zones (Wada & Wang, 2009). The maximum vertical component of the corner flow velocity on the slab is ~25% of U_{Stokes} for a diapir with a radius of 3.7 km.

Combining $\vec{U}_{Stokes}$ and $\vec{U}_C$, and knowing the depth at which a diapir of given radius R will separate from the slab, we can then calculate *P-T-t* trajectories of a diapir through the wedge. Trajectories for seven representative diapir sizes (0.67, 0.8, 1.2, 1.7, 2.4, 3.2, and 3.7 km) are calculated and superimposed on the wedge thermal structure calculated numerically from $\vec{U}_C$ (van Keken et al., 2008) (Figure 3a). In general, larger diapirs (formed from thicker buoyant layers) go unstable at shallower depths, have larger Stokes velocities, and thus follow shorter, more vertical ascent paths through the mantle wedge. By contrast, smaller diapirs initiate deeper and ascend more slowly along longer paths that undergo greater deflection in the downdip direction. The net result is that larger diapirs undergo less heating compared to smaller diapirs (Figure 3b) but ascend through the hot core of the wedge closer to the location of the volcanic arc (Figure 3c).

2.5. Numerical Scheme and Methods

Our two-phase flow model is based on deal. II (*D*ifferential *E*quation *A*nalysis ***L***ibrary) (Bangerth et al., 2007), a C++ program library targeted on the computational solution of partial differential equations using adaptive finite elements. deal. II uses the PETSc package (Balay et al., 1997) for parallel computation. Our code has recently been used to model reactive dissolution in the upwelling mantle in both 2-D and 3-D (Tirupathi et al., 2014). deal. II provides basic grid generation for a 2-D circle (https://dealii.org/8.4.0/doxygen/deal. II/step_10.html). The diapir is discretized into ~2,500 finite elements resulting in a resolution of ~110 m for a diapir with a radius of 3.7 km. The grid can be easily refined to increase the resolution.

In our numerical scheme, we first solve equation (15) for P, with the initial porosity ϕ_0. After obtaining P, we then solve the scalar potential Ψ in equation (16) for $\vec{W}^c$. After adding $\vec{W}^c$ to the analytic solution $\vec{W}^r$, we get

Table 2
Cases and Parameters

Case		Compaction length (km)	Diapir radius (km)	Boundary type[a]
Group1	CL12.8_I_R3.2	12.8	3.2	impermeable
	CL12.8_I_R3.7	12.8	3.7	impermeable
	CL12.8_I_R2.4	12.8	2.4	impermeable
	CL12.8_I_R3.2_HR	12.8	3.2	impermeable
	CL12.8_I_R3.2_Picard	12.8	3.2	impermeable
	CL5.7_I_R3.7	5.7	3.7	impermeable
	CL40.2_I_R3.7	40.2	3.7	impermeable
Group2	CL12.8_P_R3.2	12.8	3.2	permeable
	CL12.8_P_R3.7	12.8	3.7	permeable

[a]Two types boundary conditions are applied.

the solid velocity $\vec{W}$. Combining P and $\vec{W}$, we calculate the melt velocity $\vec{v}$ through equation (17). We next solve the advection-diffusion equations (equations (18) and (19)) for ϕ and T, respectively. deal. II provides a basic backward differentiation formula (BDF) scheme of order 2 (Iserles, 1996) to solve the advection-diffusion equations. The time step size is automatically adjusted based on the Courant-Friedrichs-Lewy condition. To stabilize the BDF discretization, we use an entropy viscosity method (Guermond et al., 2011). This stabilization method has been used in many codes based on deal. II [e.g., ASPECT, Heister et al., 2017]. We solve equation (18) for porosity ϕ, using the melt velocity $\vec{v}$ obtained from equation (17) and $\dot{\Gamma}$ prescribed by the temperature of previous time step in equations (11) and (12). After obtaining the new porosity, and thereafter the new Darcy flux, we solve the new temperature field in equation (19). When we solve ϕ in equation (18), we turn off the diffusion terms in the basic BDF of deal. II. Because the porosity in equation (18) is nonlinearly related to the melt velocity, compaction velocity, and temperature in equations (15), (16), and (19), we iterate on the convergence of the porosity, pressure, compaction potential, and temperature within a single time step (section 3.2 and Table 2). We find that on average seven within-time-step iterations are sufficient for convergence with a tolerance of 10^{-8} on temperature field, and our results remain unaltered. Hence, for most cases, the forward time stepping is performed without an inner iteration as this approach yields sufficient accuracy and is computationally economical. We benchmarked our approach against the solution for a propagating solitary wave (Barcilon & Richter, 1986; Richter & McKenzie, 1984). The detailed parameters and initial conditions for the benchmark can be found in the supporting information.

2.6. Boundary Conditions and Initial Conditions

For the P, $\vec{v}$, and Ψ fields, we focus on the case of an impermeable boundary and also investigate cases with a permeable boundary condition along the margins of the diapir. For cases with an impermeable boundary, the normal components of Darcy flux and rotational flow are set to 0 at the margin of the diapir ($\sqrt{x^2+z^2}=R$)

$$\vec{n}\cdot\vec{S}=\vec{n}\cdot\phi\left(\vec{v}-\vec{W}\right)=0, \tag{21}$$

$$\vec{n}\cdot\vec{W}^{r}=0. \tag{22}$$

Here $\vec{n}$ is the normal direction to the boundary pointing outward. The Stokes solution satisfies equation (22) automatically. To satisfy equation (21), we require the normal directions of melt velocity and compaction velocity to be 0

$$\vec{n}\cdot\vec{v}=0, \tag{23}$$

$$\vec{n}\cdot\vec{W}^{c}=0, \tag{24}$$

Equation (21) means

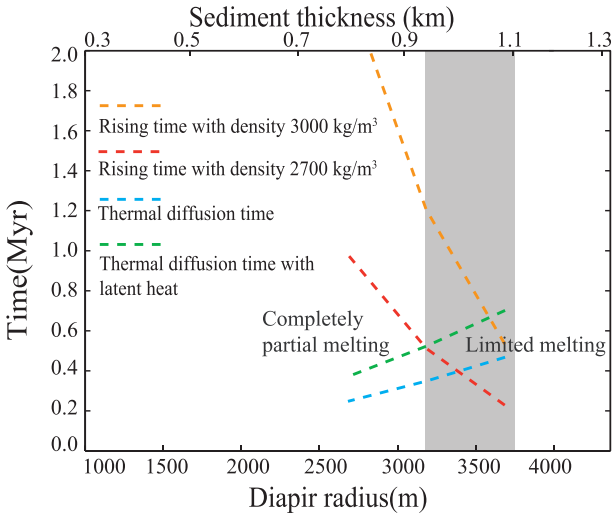

Figure 4. Scaling analysis comparing the time scales for diffusive thermal equilibrium (blue and green curves) to diapir ascent time (orange and red curves) as a function of diapir radius. The horizontal axis on top is the thickness of sedimentary layer on the slab top that will produce a diapir of a given radius (lower axis). Based on this scaling, diapirs with radii less than ~3.2 km will achieve complete thermal equilibrium and thus undergo partial melting throughout during ascent through the wedge.

$$\vec{n}\cdot\left(\nabla P-\Delta\rho g\vec{e_z}\right)=0, \text{or } \vec{n}\cdot\nabla P=\vec{n}\cdot\Delta\rho g\vec{e_z} \tag{25}$$

and under these boundary conditions equation (24) implies that

$$\frac{\partial\Psi}{\partial\vec{n}}=0. \tag{26}$$

However, equation (16) is a Poisson's equation and the applied Neumann type boundary condition is not sufficient to determine its solution. Thus, in practice, we set Ψ at the boundary point ($x = R$, $z = 0$) equal to 0.

For cases with a permeable diapir boundary, we assume the Darcy flux at the boundary is proportional to the edge porosity multiplied by the buoyancy flux

$$\vec{n}\cdot\vec{S}=\phi|_{\text{edge}}\,\vec{n}\cdot\frac{K\Delta\rho g}{\mu}\vec{e_z} \tag{27}$$

Because simulations with this boundary condition do not conserve mass (due to leakage of melt out of the diapir) we focus our discussions below on cases with an impermeable boundary; applications with a permeable boundary are discussed in section 4.1.

The porosity equation (equation (18)) also requires boundary and initial conditions. As an initial condition, we set the porosity on the boundary of the diapir equal to an assumed background porosity of 0.1% for the mantle wedge. The initial porosity within the diapir is taken to be larger than in the mantle wedge given the more fusible nature of sediments compared to mantle peridotite and we assign an initial porosity of 1% within the diapir. Sensitivity tests with an initial porosity of 0.1% in the diapir do not result in significant differences in the final porosity field. For the impermeable cases, the porosity boundary condition is imposed as zero flux. Similarly, we must set initial and boundary conditions for F in equation (13). F is initially assumed to 0 in the diapir and the impermeable and permeable cases are assigned Neumann and Dirichlet boundary conditions, respectively.

For the energy equation (equation (19)) the initial condition on temperature is set such that the entire diapir has a temperature equal to that of the subducting slab surface (T_{Ref}). The temperature boundary condition is time-dependent and follows the diapir's *P-T-t* trajectory during its ascent through the mantle wedge (Figure 3b). For example, the boundary temperature of the large (3.7 km) diapir first increases from the slab surface temperature to 1000 °C in the core of the mantle wedge, and then decreases to ~600°C at the base of the overlying lithosphere (Figure 3b). We stop our computations when the temperature drops to 700 °C, at which point all melt has recrystallized and the internal porosity structure ceases to evolve. For computational considerations, we discretize the time-dependent temperature boundary condition to a step function with 20 intervals (purple and black curves in Figure 3b) for the diapirs with radius smaller than 3.2 km and a step function with 10 intervals for the large diapir case (green curve in Figure 3b).

3. Results

Before describing our full two-phase flow solutions, we first compute scaling relationships for diapir ascent time and thermal diffusion time as a function of diapir size and buoyancy (section 3.1). Using these scalings and the predicted *P-T-t* paths shown in Figure 3, we then select a range of diapir sizes for the full two-phase flow simulations (section 3.2), which provide a more detailed estimation of the thermal and chemical evolution inside the diapir. In this section, we focus on numerical calculations with an impermeable boundary to illustrate the dynamics of melting, melt segregation, and depletion in an ascending diapir, and highlight how the full numerical solutions differ from the simple analytical scaling relations.

3.1. Scaling Solutions Without Melt Segregation

Based on the superposition of Stokes and wedge corner flow, we estimate ascent time for a range of diapir sizes assuming sediment densities of 2,700 and 3000 kg/m^3 (red & orange curves in Figure 4, respectively) and a mantle density of 3,400 kg/m^3. A sediment density of 3,000 kg/m^3 corresponds to a diapir with 30 vol% melt extraction. This estimate is calculated for relatively small degrees of melting as (2,800 * 100% − 30% * (2,800 − 500))/70%, where the density contrast between sediment and melt is assumed to be 500 kg/m^3 (Table 1). Assuming the diapir is heated along its margin at a constant high temperature corresponding to the temperature at the core of the mantle wedge, we next calculate the timescale for diffusion into the diapir as R^2/κ, where κ is the thermal diffusivity and assumed to be constant. The thermal diffusion times are calculated both with and without the effects of latent heat (green and blue curves in Figure 4). The diffusion timescale with latent heat is calculated by modifying the thermal diffusivity as $\widetilde{\kappa} = \kappa/\left(1 + \frac{L}{C_p \Delta T}\right)$, where the c_p is the heat capacity, L is the latent heat, and ΔT is the temperature difference between the sediment solidus and liquidus (e.g., Schmeling & Wallner, 2012).

The competing timescales for diapir ascent and diffusive heating allow us to quantify the general melting behavior in a rising diapir as a function of its radius. Larger diapirs will ascend more quickly and heat more slowly relative to smaller diapirs. The point where the diffusion and ascent time scales intersect (Figure 4) provides a prediction of the minimum radius of a diapir that does not undergo partial melting throughout its entire interior. This radius is ~3.4 km without including the effect of latent heat (intersection of blue and red curves) and decreases to ~3.2 km (intersection of green and red curves) when latent heat is included; diapirs formed from sedimentary layers of ~920 m will have radii of 3.2 km (Figure 3a). This analysis suggests that a diapir with a radius less than ~3.2 km will have an ascent time larger than the diffusion timescale and thus will thermally equilibrate and experience partial melting throughout during ascent through the mantle wedge. By contrast, larger diapirs that initiate farther updip on the slab surface and traverse shorter ascent paths will not experience complete partial melting throughout.

However, there are some important caveats to this simple scaling analysis. First, we assume instantaneous heating to the maximum temperature at the core of the mantle wedge throughout the entire ascent, as opposed more realistic *P-T-t* paths as shown in Figure 3. In particular, larger diapirs that detach from the slab at shallower depths will experience temperatures above the solidus along only a fraction of their ascent path. Thus, the diffusion timescale for these cases will be underestimated compared to ascent along a more realistic *P-T-t* path. Second, this analysis assumes batch melting; however, if partial melts segregate within the diapir (or escape into the surrounding mantle wedge), the residue will become more refractory, suppressing further melting. In the following sections, we address these issues using numerical simulations that explicitly simulate partial melting and two-phase flow along *P-T-t* paths appropriate for diapirs likely to contribute to arc magmas. We focus on diapirs with radii between 2.4 and 3.7 km (created from sediment layers 0.74–1.1 km thick), which traverse the core of the mantle wedge within ±25 km of the volcanic arc (assuming the arc forms above a slab depth of 100 km) (Figure 3c).

3.2. Numerical Simulations of Melting and Melt Segregation

A total of nine numerical simulations were conducted in this study (Table 2). The first group of seven cases were run using the impermeable boundary and are presented in this section. The additional two cases with a permeable boundary will be discussed in section 4.1. The first three impermeable cases correspond to diapir radii of 2.4, 3.2, and 3.7 km, respectively. The 2.4-km radius diapir evolves for ~2 Myr, which is the longest case that we simulate. In the fourth case we use a radius of 3.2 km to perform a resolution test with a factor of 2 grid refinement (~65-m resolution compared to 110-m resolution in the first three cases). The fifth case tests convergence using the within-time-step iterations described in section 2.5. All five of these cases have a compaction length δ_c = 12.8 km, equivalent to a solid shear viscosity of 5 × 10^{18} Pa·s. The final, two impermeable cases test the influence of compaction length assuming a 3.7-km diapir and δ_c = 5.7 km (η = 1 × 10^{18} Pa·s) and δ_c = 40.6 km (η = 5 × 10^{19} Pa·s), respectively. We adopt a labeling scheme for these model runs based on the compaction length (CL), the boundary condition (I = impermeable; P = permeable), and the diapir radius (R) (Table 2). For example, CL12.8_I_R3.2 refers to a case with a compaction length of 12.8 km, an impermeable boundary, and a diapir radius of 3.2 km, while

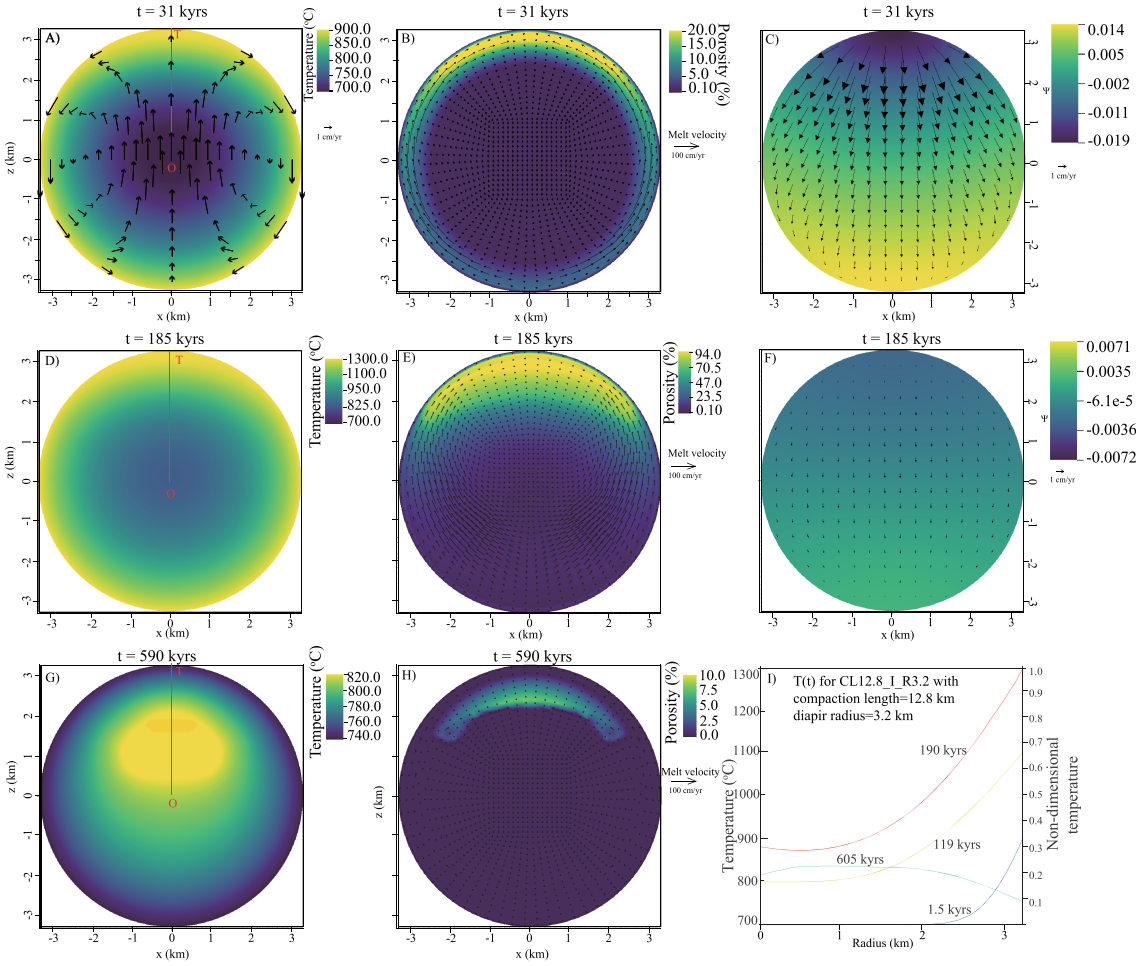

Figure 5. Snapshots of (a, d, and g) temperature, (b, e, and h) porosity and melt velocity, and (c, f) compaction potential and compaction velocity for an impermeable diapir with a radius of 3.2 km and a compaction length of 12.8 km (CL12.8_I_R3.2). Model results at time steps of 31, 185, and 590 kyr are shown, where 185 kyr corresponds to the peak temperature conditions at the core of the mantle wedge. The rotational flow is also plotted in (a) for comparison. The temperature evolution along the profile OT in (a) is plotted in panel (i).

CL12.8_P_R3.7 refers to a case with a compaction length of 12.8 km, a permeable boundary, and a diapir radius of 3.7 km.

To illustrate the basic dynamics of a melting diapir, we start by describing case CL12.8_I_R3.2 with an impermeable boundary and an intermediate radius of 3.2 km. The initial state is allowed to evolve for 800 kyr following the time-dependent temperature boundary condition associated with a diapir ascent path assuming a sediment density of 2,800 kg/m^3 (Figure 3b and Table 1). The temperature at the boundary of the diapir increases from the initial value of 700 to 900 °C over the first ~31 kyr of the simulation. This results in heating of the diapir interior through thermal diffusion (Figure 5a). As temperatures increase, melting occurs, resulting in a circular channel of high porosity along the boundary of the diapir (Figure 5b). Pressure gradients drive the melt from regions of high pressure to regions of low pressure as expressed by the fluid velocity (Figure 5b). Due to the induced pressure gradient, melt in the lower portion of the diapir first flows downward, overcoming buoyancy, and into the high porosity channel. Thereafter, the melt migrates under its buoyancy through the high porosity channel to the top of the diapir. Focusing of the melt migration within the channel occurs due to the porosity dependence of the permeability (equation (4)). Advective heating associated with melt migration is relatively small because the melt velocities are roughly parallel to the boundary (Figure 5b).

In response to the upward migration of melt, the diapir matrix contracts downwards due to compaction (Figure 5c). This downward compaction-induced flow is slightly stronger than the central upward

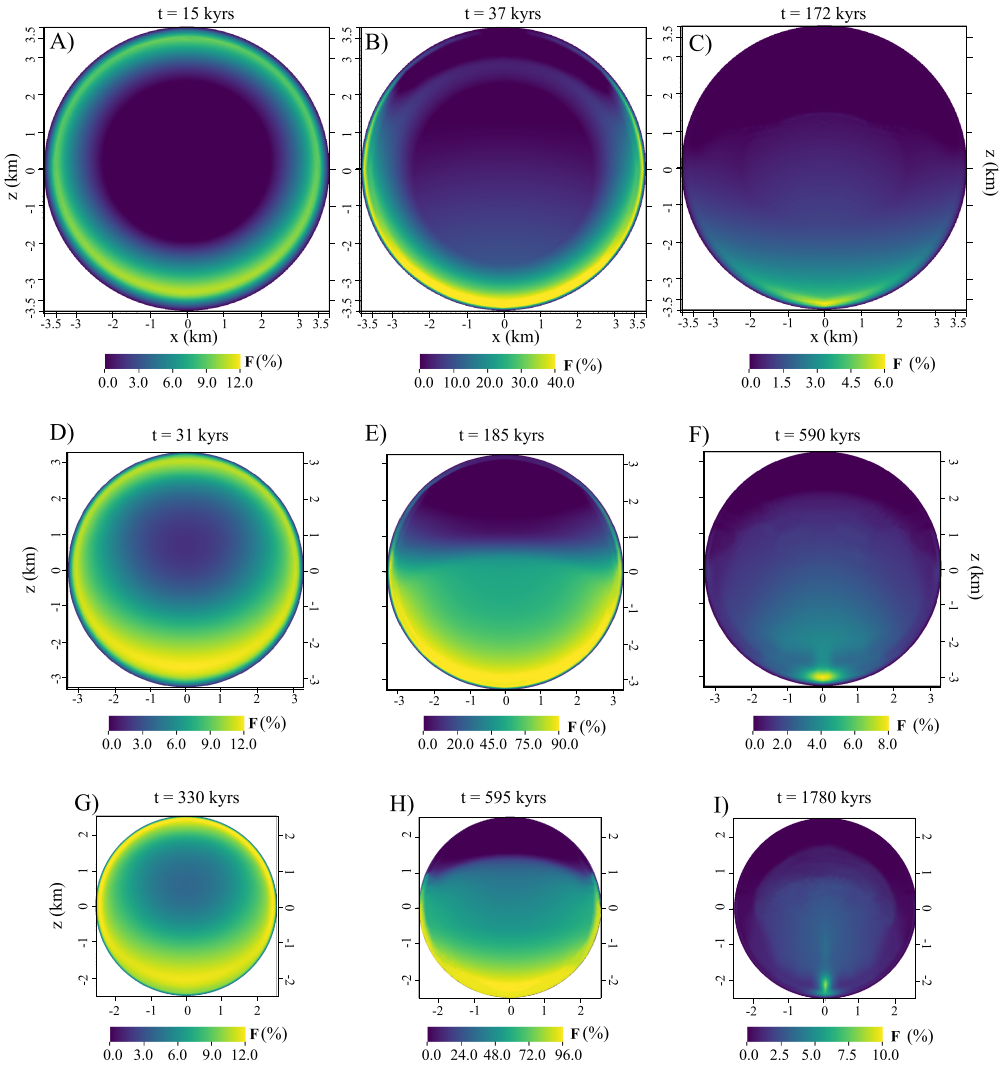

Figure 6. Evolution of depletion (F in %) as a function of time for three different sized diapirs: (a–c) 3.7 km, (d–f) 3.2 km, (g–i) 2.4 km. All calculations assume a compaction length of 12.8 km and an impermeable boundary condition. The *P-T-t* trajectories for these diapirs are shown as the green, purple, and solid black curves in Figure 3b.

rotational flow induced by shear on the margins of the diapir (Figure 5a). After ~185 kyr of ascent, the boundary temperature approaches the maximum wedge temperature of 1300 °C (Figures 3b and 5d), and the porosity reaches 94% near the top of the domain (Figure 5e). As temperatures reach their maximum value, melt collection at the top of the diapir slows and downward compaction of the matrix becomes smaller (Figure 5f), eventually allowing the solid flow field to be dominated by the rotational flow (Figure 5a). After the diapir has ascended through the hottest part of the mantle wedge it begins to cool (Figure 5g), leading to crystallization and reduced porosity (Figure 5h). The temperature evolution along the radial profile OT (Figure 5a) is shown in Figure 5i.

To ensure that our numerical resolution is sufficient to resolve the melting dynamics within the diapir, we ran a higher resolution case (CL12.8_I_R3.2_HR) with twice the grid resolution, but keeping all other parameters equal. The results, especially for porosity, are very similar to case CL12.8_I_R3.2, implying that our grid is sufficient to resolve melting and melt segregation. In addition, although our pressure condition (equations (21) and (22)) should guarantee 0 Darcy flux, we also tested a Neuman and Dirichlet boundary condition for the porosity field and found almost identical porosity fields.

We next examined the case of a larger 3.7-km diapir (Case CL12.8_I_R3.7; Table 2), which initiates farther updip on the slab surface and rises faster through a shallower portion of the mantle wedge, reaching the base

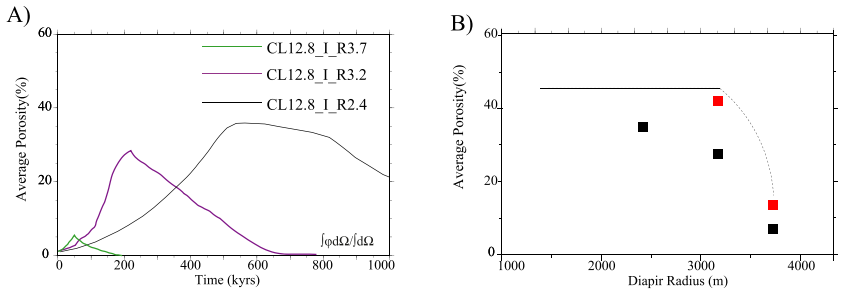

Figure 7. (a) Evolution of the average porosities for three impermeable cases CL12.8_I_R3.7, CL_12.8_I_R3.2, and CL12.8_I_R2.4 shown in Figure 6. In the impermeable cases, the average depletion equals to the average porosity. (b) Maximum average porosity as a function of diapir radius for cases with an impermeable boundary (black symbols) and permeable boundary (red symbols). The average porosity is equal to the average depletion for impermeable cases. The depletion upper bound (black curve) from the scaling calculations is predicted using $[T_M - T_s(F)]/(T_L - T_s) = F$. T_M is the maximum mantle wedge temperatures a diapir passes through.

of the overlying lithosphere in ~180 kyr (green curve in Figure 3b). Because the larger diapir rises faster and ascends through a cooler mantle column, it experiences less heating along its boundary, and thus, the porosity increases more slowly compared to the smaller 3.2-km diapir case. The larger diapir aggregates a maximum porosity of only ~39% at the top of the diapir (Figure S2b), much lower than the maximum porosity of 94% for the 3.2-km diapir (Figure 5e). Finally, we compared these two simulations to an additional case with a radius of 2.4 km. The 2.4-km diapir detaches from the slab at 120-km depth and due to its smaller size (and correspondingly smaller ascent rate) takes ~1.8 Myr to reach at the base of the lithosphere (Figure 3). This case is the longest one we can compute in our cluster. This smallest case results in the largest maximum porosity just under 100% as the diapir ascends through the core of the mantle wedge.

Regardless of diapir size, all cases are initially characterized by a rim of high depletion along the margin of the diapir (Figure 6). As the diapirs continue to ascend several effects lead to segregation of more depleted material near the bottom of the diapir and less depleted material at the top. First, the downward component of solid flow induced by compaction causes the more depleted regions formed near the boundary to advect downward (Figures 6b, 6e, and 6h). After passing though the core of the mantle wedge, the downward compaction becomes smaller, but the rotational flow continues to advect the depleted regions along the boundary downward. Because smaller diapirs take longer to ascend (Figures 3a and 3b), their interiors experience more overturn flow (Figure 1b), homogenizing the distribution of depletion distribution compared to the larger diapirs (Figures 6f and 6i). In addition, recrystallization leads to refertilization of the residue. This effect is particularly pronounced near the top of the diapir, where melt accumulation causes the local melt fraction to exceed the equilibrium melt fraction and drive recrystallization (equation (11)) even before the diapir has reached the core of the mantle wedge (Figure 6).

At the end of the ascent path, we find all three diapirs to be only slightly depletsed near their base (6–10%) (Figures 6c, 6f, and 6i), though the maximum degree of melting may exceed 90% at the core of the mantle wedge (~96% for case CL12.8_I_R2.4; Figure 6h).

We can also quantify the average depletion within the diapir ($\overline{F} = \frac{\int F d\Omega}{\int d\Omega}$) through time, where Ω represents the total area of the diapir. With an impermeable boundary, the average depletion is equivalent to the average porosity ($\overline{\phi} = \frac{\int \phi d\Omega}{\int d\Omega}$) (see Appendix A in Schmeling et al., 2019). The shorter and colder ascent path followed by the 3.7-km diapir (case CL12.8_I_R3.7) results in a maximum average depletion of only ~6% (green line in Figure 7a). By contrast, the longer heating paths experienced by the 3.2- and 2.4-km radius diapirs result in maximum average porosities of 29% and 37%, respectively (Figure 7b).

We plot the average melt fraction predicted by the scaling relation (Figure 4) and the numerically calculated maximum average depletions in Figure 7b. The average melt fraction predicted by the scaling is 46% for a diapir that is thermally equilibrated with a mantle temperature of 1300 °C, or partial melting throughout

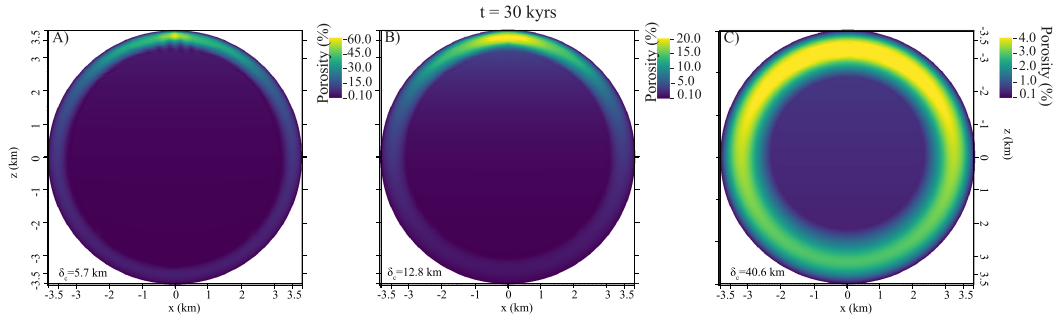

Figure 8. Effect of compaction length on the formation of the high porosity channel. Color maps show porosity fields from cases with a compaction length of (a) 5.7 km, (b) 12.8 km, and (c) 40.6 km for a model time of 38 kyr.

(solid black line in Figure 7b). Larger diapirs do not undergo complete thermal equilibration and the predicted melt fractions decrease, reaching only 13% for 3.7-km diapir (dashed curve in Figure 7b). The maximum average melt fractions in our numerical models (black squares in Figure 7b) are lower because the diapirs are only exposed to a temperature of 1300 °C along a short portion of their ascent path (Figure 3). Indeed, even case CL12.8_I_R2.4, which has a radius smaller than the critical size predicted for complete thermal equilibration, does not achieve the theoretical average melt fraction (solid black line in Figure 7b).

Finally, to test the influence of compaction length on melt migration, we used the 3.7-km radius diapir and ran two more cases with compaction lengths of 5.7 km (CL5.7_I_R3.7) and 40.6 km (CL40.6_I_R3.7), respectively. The general pattern of melt segregation is similar for all three compaction lengths, with the most important difference between these cases being the width of the high porosity channel that develops along the margin of the diapir (Figure 8). For smaller compaction lengths, the width of the high porosity channel decreases, while the maximum porosity increases.

4. Discussion

In this study we have quantified the melting and depletion histories of a chemically fertile sedimentary diapir (Figure 7). We focus on sedimentary diapirs whose ascent paths promote melting in the portion of the mantle wedge most likely to contribute to arc magmatism. Ascent paths calculated from the superposition of mantle wedge corner flow and buoyant Stokes flow show that sediment layers 0.74–1.1 km thick will go unstable and form diapirs with radii of 2.4–3.7 km that traverse the mantle wedge within ~25 km of the volcanic arc. Our two-phase flow simulations show that as a diapir of these dimensions ascends from the slab toward the core of the mantle wedge, melting along the boundary results in a high porosity rim that focuses melt toward the top of the diapir, while the bottom half of the diapir becomes increasing depleted. This results in a heterogeneous pattern of depletion by the time the diapir reaches the core of the mantle wedge, ranging from 1–2% depletion at the center of the top-half diapir to just under 100% near diapir base. The average depletion of the diapir, however, is significantly lower than the maximum depletion preserved in the residue. Further, because melt cannot leave the diapir in the impermeable cases presented above, recrystallization leads to refertilization as the diapir transits the upper half of the mantle wedge.

In general, our results are consistent with earlier studies (e.g., Katz & Rudge, 2011; Sleep, 1984). Assuming energy conservation, Katz and Rudge (2011) found a rising circular heterogeneity with radius of ~1 km would reach melt fractions of 35–82%. For comparison, our smallest diapir case (R = 2.4 km) produces a maximum average melt fraction of 36% (Figure 7). We note that our model differs from Katz and Rudge (2011) in that we neglect adiabatic melting. This assumption is justified because adiabatic melting over the length of the mantle wedge is much smaller than the effects of thermal diffusion and decompression melting. Based on the parameters used here, the decompression melting and thermal melting rates are ~0.07%/kyr and 0.3%/kyr, respectively. By contrast, adiabatic melting gives rise to a melting rate of only 0.004%/kyr.

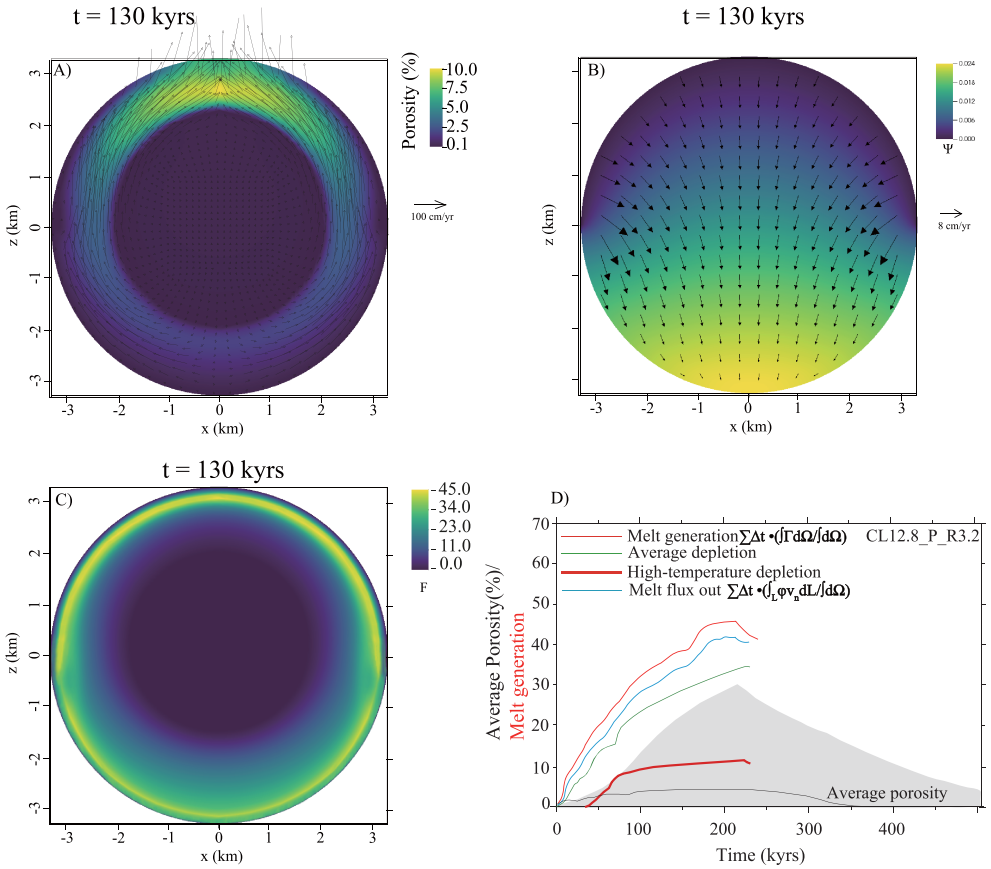

Figure 9. Snapshots of (a) porosity and melt velocity, (b) compaction, and (c) depletion for a permeable diapir with a radius of 3.2 km (CL12.8_P_R3.2). (d) Total melt generation (thin red curve), melt flux out of the diapir (blue curve), average depletion (green curve), and average porosity (black curve) as a function of time. The shadow areas are the average porosities from the corresponding impermeable case (CL12.8_I_R3.2) shown in Figure 7a. The high-temperature depletion (1050 °C solidus) evolution is included as the thick red curve.

4.1. Comparison to Simulations With a Permeable Boundary

As our impermeable cases show, a large amount of melt accumulates at the top of the diapir during ascent. Such a high melt fraction will generate a large overpressure at the top boundary, which tends to force melt into the surrounding mantle. To address this issue, we present calculations from two additional cases with permeable boundaries (Table 2) corresponding to diapir radii of 3.2 and 3.7 km and a compaction length of 12.8 km (CL12.8_P_R3.2 and CL12.8_P_R3.7, respectively). We apply the permeable boundary condition described in equation (28), which allows melt (and hence mass) to flow out of the diapir. In these cases, mass is not conserved resulting in excess compaction. This excess compaction due to the outward melt flux could flatten the diapir by up to a factor of approximately one third, changing the general shape of a sphere. With this caveat in mind we use the melt and depletion patterns as a first-order indication of how escape of melt into the surrounding mantle will influence the evolution of melt segregation and depletion in the diapir.

To track the overall melting and depletion history of the permeable diapir cases, we quantify average total melt generation ($\overline{\Gamma} = \sum_t \Delta t \cdot \left(\int_{area} \dot{\Gamma} d\Omega / \int_{area} d\Omega \right)$), the total melt flux out of the diapir ($Q = \sum_t \Delta t \cdot \oint \left[(\varphi \vec{v})|_l \cdot \vec{n} \right] dl / \int_{area} d\Omega$), average depletion ($\overline{\Gamma} = \int_{area} F d\Omega / \int_{area} d\Omega$), and average porosity, where Ω and l represent the area and circumference of the diapir, respectively. For the two permeable boundary cases, the average melt generation is not balanced by the average porosity due to the melt flux out of the diapir (Figures 9d and 10d). We quantify melt extraction within the permeable diapir by calculating depletion

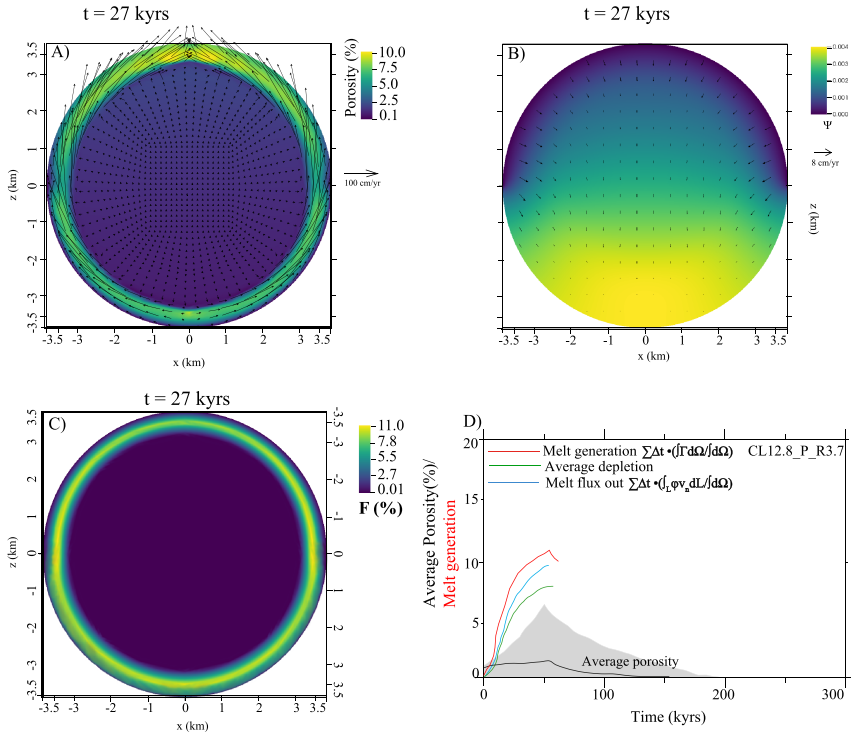

Figure 10. Snapshots of porosity and melt velocity (a), compaction (b), and depletion (c) from the permeable big diapir case (CL12.8_P_R3.7). The total melt generation, the melt flux out, average depletion, and average porosity are shown for permeable large diapir case (d). The shadow areas are the average porosities from the impermeable big case as in Figure 7a.

through the peak temperature on the ascent path. We stop our depletion calculation at the core of the mantle wedge where the boundary temperature begins to decrease because we cannot track freezing of melt that has left the diapir.

Overall, the permeable cases show a similar pattern of melt segregation compared to the cases with an impermeable boundary. Porosity increases near the margin of the diapir as it ascends from the slab surface toward the hot core of the mantle wedge (Figures 9a and 10a). However, in comparison to the corresponding impermeable cases (Figure 5b), the permeable diapirs show a more gradual increase in porosity due to melt escaping out of the top of the diapir, with the local porosity never exceeding ~10% (Figures 9a and 10a). The escape of melt results in higher melt velocities near the top of the diapir and enhances the compaction (Figure 9b) along the top hemispherical boundary of the diapir; the melt velocities in the bottom half of the diapir remain very similar to the impermeable case. This difference is caused by the larger pressure gradient (and hence Darcy velocity) at the boundary in the permeable cases. The larger permeable diapir in case CL12.8_P_R3.7 (Figure 10) shows similar behavior, but with less overall compaction (Figure 10b) and depletion (Figure 10c) due its cooler and more rapid ascent path.

The average porosity in case CL12.8_P_R3.2 reaches a maximum of only 4% (black curve in Figure 9d) compared to 31% for the corresponding impermeable case CL12.8_I_R3.2 (Figure 7). By contrast, the average total melt generation is greater in the permeable case (reaching a maximum of 43%) compared to the impermeable case (29%) (thin red curve in Figure 9d). The difference in total melt generation in the permeable case is caused by the lower porosities resulting from the outward melt flux (blue curve in Figure 9d), which leads to an enhanced melting (equation (11)). The compaction in the permeable cases (Figure 9b) is greater than that in the impermeable cases (Figure 5c). Moreover, the difference between the melt generation and the average porosity in the permeable case reflects the large volume of melt is lost out of the diapir (compare blue and black curves in Figure 9d). The decrease in melt generation after ~195 kyr (Figure 9d) corresponds to the period in which the boundary temperature begins to decrease, and freezing occurs within the diapir.

Table 3
Predicted Compositions in the Melt at the Maximum Average F

Pressure/depth (GPa)	1.78/55 km (3.7 km)[a]	2.9/90 km (3.2 km)	3.4/105 km (2.4 km)
Degree of melt (F)[b]	0.06	0.3	0.35
SiO_2	73.87	73.25	72.84
TiO_2	0.27	0.40	0.43
Al_2O_3	14.87	15.44	15.55
FeO	0.59	1.06	1.24
MgO	0.12	0.25	0.32
CaO	0.50	1.02	1.11
Na_2O	5.63	3.58	3.22
K_2O	4.14	4.95	5.24
K_2O/Na_2O	0.74	1.38	1.63

[a]Numbers in brackets are the radii for corresponding diapirs. [b]All the water contents are assumed as 2 wt% (Schmidt, 2015).

The average depletion in permeable case CL12.8_P_R3.2 reaches a maximum value of ~35%, which is slightly higher than maximum average depletion of 31% in the corresponding impermeable case (green curve in Figure 9d). However, the escape of melt results in a very different spatial pattern of depletion. As discussed above, the impermeable diapirs develop a highly depleted lower hemisphere and a relatively undepleted upper hemisphere, where crystallization of rising melts refertilizes the upper portions of the diapir. By contrast, permeable diapirs develop a depleted rim that coincides with the region of melting. This occurs because the rising melts do not pool and recrystallize at the top of the diapir and thus the original pattern of depletion is retained until internal convection within the diapir redistributes the depleted material.

In addition to calculating total depletion within the diapir using the sediment solidus described above, we also calculate a "high-temperature" depletion that tracks only regions where the temperature exceeds 1050 °C. This choice is motivated by the results of Behn et al. (2011), who found that only ultra-high-pressure (UHP) metasediments that had experienced temperatures greater than 1050 °C had lost key trace elements characteristic of the sediment signature in arc lavas. Because the temperature remains less than 1050 °C on the early portion of the ascent path, there is significantly less high temperature depletion compared to average depletion. Indeed, while the central regions of the diapir undergo melting in cases CL12.8_P_R3.2 and CL12.8_P_R3.7, they never exceed temperatures of 1050 °C. At the peak boundary temperature (1300 °C), the total and high-temperature depletion reach their maximum values of ~34% and 11%, respectively.

4.2. Implications for Sediment Melting in Subduction Systems

The calculations presented here have important implications for chemical fractionation and mass transport in subduction zones. For example, our calculations show that thick sediment layers, which become unstable at relatively shallow depths on the slab top, will generate large diapirs that ascend rapidly along relatively cool *P-T-t* paths through the mantle wedge. These resultant diapirs undergo relatively little melting and chemical fractionation during their ascent. In this scenario, mass transport is primarily in the form of solid material flow that emplaces fertile, relatively unmelted sediments at the base of the crust—termed relamination by Hacker et al. (2011). Generation of the arc sediment signatures in this end-member scenario requires subsequent reheating of this sedimentary material (to temperatures in excess of 1050 °C) in the lower crust. By contrast, thinner sediment layers that go unstable at greater depths on the slab top, will produce smaller diapirs that ascend more slowly along longer, hotter *P-T-t* paths. These smaller diapirs will undergo more extensive melting (at higher temperatures) as they thermally equilibrate with the mantle wedge during their ascent. In this case, the dominant process by which a sediment signature is imparted to arc volcanoes is likely through melt escaping from the diapir and transiting the mantle wedge by porous flow (e.g., Behn et al., 2011).

We can estimate the composition of melts that results from ascending diapirs based on the history of melting along their ascent path. To do so, we follow the parameterization of Schmidt (2015), who estimates major element composition as a function of the melt fraction and the pressure of melting. We assuming fluid absent melting with 2 wt% H_2O in the sediment protolith. This scenario is appropriate for melting of

hydrous sediments in an ascending sediment diapir that is not fluxed with additional fluids from below (Schmidt, 2015). Calculations are performed for the three impermeable diapir cases: CL12.8_I_R2.4, CL12.8_I_R3.2, and CL12.8_I_R3.7 and the melt compositions are presented at the point at which the diapir reaches the hottest point on its ascent path (Table 3). As discussed by Mann and Schmidt (2015) the major element composition of sediment melts remains relatively constant, with the greatest variability in the alkali elements. In particular, the K_2O/Na_2O wt-ratio is sensitive to the pressure of melting and the average melt fraction. We find that this ratio varies by more than a factor of 2 between the largest and smallest diapirs considered (0.74 to 1.63 for diapir radii of 3.7 and 2.4 km, respectively). By contrast SiO_2 content varies by ~1 wt% and Al_2O_3 varies by ≤1 wt% (see Table 3). This implies that changes in the alkali ratio of observed melts may provide the best diagnostic for determining the ascent path and melting conditions in sediment diapirs.

Finally, while not addressed in this study, if diapir buoyancy decreases in response to the depletion (e.g., Hacker et al., 2011), melting will be enhanced due to the slower ascent rates, which scale with the density contrast between the diapir and ambient mantle. Experiments compiled by Hacker et al. (2011) predict a sediment residue density of 3,000–3,300 kg/m^3 after 20–50% melting and depending on the starting composition. For a density of 3,100 kg/m^3, the Stokes velocity for a rising diapir (equation (20)) will be reduced by ~56% compared to our calculations assuming an unmelted sediment density of 2,700 kg/m^3. This effect could result in diapirs stagnating in the mantle wedge and increasing the amount of melting they undergo at higher pressures. In extreme cases where the upward Stokes velocity becomes smaller than the downward mantle wedge velocity driven by the subducting slab, the sediment residues could be dragged into the deep mantle and only melts moving by porous flow would ascend to the surface.

4.3. Limitations of our Models and Future Directions

Our model simulates a diapir as a fixed 2-D circle that does not undergo shape changes during its ascent. Based on our calculations of the solid compaction (Figures 5c, 9b, and 10b), this assumption may not be true. For example, when the ambient temperature of CL12.8_P_R3.2 is increasing during the first 180 kyr of ascent (Figure 3b), the calculated compaction velocities are downward. Such vertical magnitude of compactions (Figure 5c) can promote collapse of the solid diapir matrix into a flattened ellipse shape during this 180 kyr. Our current model is thus adequate for tracing internal melt segregation assuming the diapir undergoes small amounts of deformation. This assumption is most accurate for cases with an impermeable boundary and larger diapirs that undergo less total melting. Further, pressure variations and solid flow inside the diapir caused by the mantle wedge corner flow are ignored in our models as we incorporate only the pressure and solid flow induced by the Stokes flow (section 2.4). Future studies should develop models that (1) couple deformation of the diapir and mantle wedge (e.g., Hasenclever et al., 2011; Zhu et al., 2011) and (2) capture melt transport from the diapir into the wedge in order to better quantify melt segregation processes in rising diapirs. In addition, such models would provide constraints on the cooling effects of diapirs on the ambient thermal structure of the mantle wedge.

Compared to the geometry approximation of a 2-D circle, a 2-D axisymmetric sphere is a better approximation though it is not easy to implement with deal. II. More accurate analytic solutions of thermal conduction for cylinder and sphere (Cengel, 2006) show that the thermal diffusion time in a sphere is only ~68% of that in a cylinder with the same radius. Hence, our assumed 2-D circle approximation overestimates the timescale for diffusive equilibrium between the diapir and mantle wedge, implying that melt generation will be enhanced in a 3-D sphere compared to the calculations presented here.

Finally, while this study represents a first step in quantifying melting processes in rising chemically fertile sediment diapirs, much work remains to fully model the melts and residues of this process and how they are emplaced in arc settings. For example, our model framework is not able to track melts after they leave the diapir. Future studies are therefore required to understand how such melts ascend and enter the volcanic plumbing system of arcs. Moreover, additional modeling efforts are required to quantify the fate of the solid residue of a diapiric melting process and its emplacement into the base of arc crust. Our work demonstrates that these residues could be geochemically heterogeneous with highly depleted rims and enriched interiors when diapirs arrive at the hottest portion of wedge, as in this case leakage of melt is a realistic scenario. Preservation of such features in arc settings could therefore provide additional evidence of active diapirism in subduction settings.

5. Conclusions

1. Using instability analyses we predict that the radii of sedimentary diapirs arising from sediment layers 0.2–1.1 km thick are between 0.7 and 3.7 km, and diapirs with radii between 2.4 and 3.7 km will ascend and melt within 25 km of the volcanic arc at subduction zones. Smaller diapirs will detach farther downdip on the slab surface leading to ascent paths that do not transit the mantle wedge beneath the volcanic arc.
2. Numerical two-phase flow calculations indicate that diffusive heating of a sedimentary diapir as it ascends through the hot corner of the mantle wedge will produce melts that form an annular channel of high porosity and high permeability along the margin of the diapir. As the diapir heats during ascent into the hot core of the mantle wedge, new melts are focused into this channel, migrating upward and accumulating near the top of the diapir. Melt segregation is driven primarily by the pressure difference between the high porosity channel and the low porosity interior. Such a high porosity annular melt channel leads a strong depletion gradient from the central portion of the diapir to the exterior. During ascent, depletion variations induced by the melt channel can range from 1–2% near the center, to just under ~100% near the base of the diapir. For an impermeable diapir, the depletion heterogeneity is homogenized in the final crystallization stage. Permeable diapirs would flatten due to loss of melt to the surrounding mantle, but the residue would retain an annular pattern of depletion.
3. Our numerical results indicate that most diapirs (even those that thermally equilibrate with the hot core of the mantle wedge) do not undergo complete melting and indeed have lower average melt fractions than predicted from simple scaling analyses for thermal diffusion. Diapirs whose ascent paths favor melting beneath the volcanic arc will undergo no more ~40–50% total melting. Further only 10–30% melting occurs at temperatures >1050 °C required to generate the sediment signature in arc lavas.
4. In summary, thick sediment layers generate large diapirs that ascend rapidly along relatively cool *P-T-t* paths through the mantle wedge. The resultant diapirs undergo relatively little melting and chemical fractionation during their ascent, leading to the relamination of relatively unmelted sediments at the base of the crust. By contrast, smaller diapirs that ascend more slowly along longer, hotter *P-T-t* paths will undergo more extensive melting (at higher temperatures). In this scenario, a sediment signature can be imparted to arc volcanoes through melt escaping from the diapir and transiting the mantle wedge by porous flow.

Acknowledgments
We thank careful reviews by Juliane Dannberg, Harro Schmeling, and Bernhard steinberger. This work is supported by NSF-1316333 (MB & NZ), NSF-1551023 (MB), NSF-1316310 (CK), and by China's Thousand Talents Plan (2015) and NSFC-41674098 funding to NZ. The public data repository of Deal.ii (www.dealii.org) is thanked for distributing the software and examples that are used in this study. Computational work was conducted in High-performance Computing Platform of Peking University, Kenny cluster of WHOI, and Pawsey Supercomputing Centre of Western Australia. We thank Timo Heister and Juliane Dannberg for deal.II technical assistance. The data of mantle wedge thermal structure and diapir trajectories, and the source code to compute the model results are available in the Mendeley data (http://dx.doi.org/10.17632/73n8zkc68s.1).

References

Balay, S., Gropp, W. D., McInnes, L. C., & Smith, B. F. (1997). Efficient management of parallelism in object oriented numerical software libraries. In E. Arge, A. M. Bruaset, & H. P. Langtangen (Eds.), *Modern Software Tools in Scientific Computing* (pp. 163–202). Boston: Springer.

Bangerth, W., Hartmann, R., & Kanschat, G. (2007). deal. II—A general-purpose object-oriented finite element library. *ACM Transactions on Mathematical Software (TOMS)*, *33*(4), 24–es. https://doi.org/10.1145/1268776.1268779

Barcilon, V., & Richter, F. M. (1986). Nonlinear waves in compacting media. *Journal of Fluid Mechanics*, *164*, 429–448. https://doi.org/10.1017/S0022112086002628

Batchelor, G. K. (1967). *An introduction to fluid dynamics*. Cambridge: Cambridge University.

Bazhan, I., Litasov, K., Ohtani, E., & Ozawa, S. (2017). Majorite-olivine–high-Ca pyroxene assemblage in the shock-melt veins of Pervomaisky L6 chondrite. *American Mineralogist*, *102*, 1279–1286.

Behn, M. D., Hirth, G., & Kelemen, P. B. (2007). Trench-parallel anisotropy produced by foundering of arc lower crust. *Science*, *317*(5834), 108–111. https://doi.org/10.1126/science.1141269

Behn, M. D., Kelemen, P. B., Hirth, G., Hacker, B. R., & Massonne, H.-J. (2011). Diapirs as the source of the sediment signature in arc lavas. *Nature Geoscience*, *4*(9), 641–646. https://doi.org/10.1038/ngeo1214

Castro, A., & Gerya, T. (2008). Magmatic implications of mantle wedge plumes: Experimental study. *Lithos*, *103*, 138–148.

Cengel, Y. A. (2006). *Heat and mass transfer: A practical approach* (3rd ed.). New York, NY: McGraw-Hill. 10020.

Clift, P., & Vannucchi, P. (2004). Controls on tectonic accretion versus erosion in subduction zones: Implications for the origin and recycling of the continental crust. *Reviews of Geophysics*, *42*, RG2001. https://doi.org/10.1029/2003RG000127

Cruz-Uribe, A., Marschall, H., Gaetani, G., & LeRoux, V. (2018). Generation of alkaline magmas in subduction zones by partial melting of mélange diapirs–An experimental study. *Geology*, *46*(4), 343–346.

Currie, C., Beaumont, C., & Huismans, R. (2007). The fate of subducted sediments: A case for backarc intrusion and underplating. *Geology*, *35*(12), 1111. https://doi.org/10.1130/g24098a.1

Dannberg, J., & Heister, T. (2016). Compressible magma/mantle dynamics: 3-D, adaptive simulations in ASPECT. *Geophysical Journal International*, *207*, 1343–1366.

Elliott, T., Plank, T., Zindler, A., White, W., & Bourdon, B. (1997). Element transport from slab to volcanic front at the Mariana arc. *Journal of Geophysical Research*, *102*, 14,991–15,019.

Gerya, T. V., & Yuen, D. (2003). Rayleigh-Taylor instabilities from hydration and melting propel "cold plumes" at subduction zones. *Earth and Planetary Science Letters*, *212*(1-2), 47–62.

Ghods, A., & Arkani-Hamed, J. (2002). Effects of melt migration on the dynamics and melt generation of diapirs ascending through asthenosphere. *Journal of Geophysical Research*, *107*, 2026. https://doi.org/10.1029/2000JB000070

Gorczyk, W., Gerya, T., Connolly, J., Yuen, D., & Rudolph, M. (2006). Large-scale rigid-body rotation in the mantle wedge and its implications for seismic tomography. *Geochemistry, Geophysics, Geosystems*, *7*, Q05018. https://doi.org/10.1029/2005GC001075

Guermond, J.-L., Pasquetti, R., & Popov, B. (2011). Entropy viscosity method for nonlinear conservation laws. *Journal of Computational Physics*, *230*(11), 4248–4267.

Hacker, B., Kelemen, P., & Behn, M. (2011). Differentiation of the continental crust by relamination. *Earth and Planetary Science Letters*, *307*, 501–516.

Hacker, B., Luffi, P., Lutkov, V., et al. (2005). Near-ultrahigh pressure processing of continental crust: Miocene crustal xenoliths from the Pamir. *Journal of Petrology*, *46*, 1661–1687.

Hall, P., & Kincaid, C. (2001). Diapiric flow at subduction zones: A recipe for rapid transport. *Science*, *292*(5526), 2472–2475. https://doi.org/10.1126/science.1060488

Hasenclever, J., Phipps, M. J., Hort, M., & Rupke, L. H. (2011). 2D and 3D numerical models on compositionally buoyant diapirs in the mantle wedge. *Earth and Planetary Science Letters*, *311*, 53–68.

Havlin, C., Parmentier, E. M., & Hirth, G. (2013). Dike propagation driven by melt accumulation at the lithosphere–asthenosphere boundary. *Earth and Planetary Science Letters*, *376*, 20–28.

Hawkesworth, C. J., Turner, S. P., McDermott, F., Peate, D. W., & van Calsteren, P. (1997). U_Th isotopes in arc magmas: Implications for element transfer from the subducted crust. *Science*, *276*(5312), 551–555. https://doi.org/10.1126/science.276.5312.551

Heister, T., Dannberg, J., Gassmöller, R., & Bangerth, W. (2017). High accuracy mantle convection simulation through modern numerical methods–II: Realistic models and problems. *Geophysical Journal International*, *210*(2), 833–851.

Hier-Majumder, S., Ricard, Y., & Bercovici, D. (2006). Role of grain boundaries in magma migration and storage. *Earth and Planetary Science Letters*, *248*, 735–749.

Hirschmann, M. (2001). Mantle solidus: Experimental constraints and the effects of peridotite composition. *Geochemistry, Geophysics, Geosystems*, *1*, 2000GC000070. https://doi.org/10.1029/2000GC000070

Hirth, G., & Kohlstedt, D. L. (2004). Rheology of the upper mantle and the mantle wedge: A view from the experimentalists. In J. Eiler (Ed.), *Inside the Subduction Factory, Geophysical Monograph Series* (Vol. 138, pp. 83–105). Washington, DC: American Geophysical Union.

Irifune, T., Ringwood, A. E., & Hibberson, W. O. (1994). Subduction of continental crust and terrigenous and pelagic sediments: An experimental study. *Earth and Planetary Science Letters*, *126*(4), 351–368. https://doi.org/10.1016/0012-821X(94)90117-1

Iserles, A. (1996). *A first course in the numerical analysis of differential equations*. Cambridge: Cambridge University Press.

Ivanovich, M., & Harmon, R. S. (1982). *Uranium-series disequilibrium*. Oxford, England: Clarendon Press.

Jull, M., & Kelemen, P. B. (1999). On the conditions for lower crustal convective instability. *Journal of Geophysical Research*, *106*, 6423–6446.

Katz, R. (2003). A new parameterization of hydrous mantle melting. *Geochemistry, Geophysics, Geosystems*, *4*, 1073. https://doi.org/10.1029/2002GC000433

Katz, R. (2008). Magma dynamics with the enthalpy method: Benchmark solutions and magmatic focusing at Mid-ocean Ridges. *Journal of Petrology*, *49*, 2099–2121.

Katz, R., & Rudge, J. (2011). The energetics of melting fertile heterogeneities within the depleted mantle. *Geochemistry, Geophysics, Geosystems*, *12*(10), n/a. https://doi.org/10.1029/2011GC003834

Katz, R. F., & Weatherley, S. M. (2012). Consequences of mantle heterogeneity for melt extraction at mid-ocean ridge. *Earth and Planetary Science Letters*, *335*, 226–237.

Kelemen, P., Hanghøj, K., Greene, A., Rudnick, R., Holland, H., & Turekian, K. (2003). One view of the geochemistry of subduction-related magmatic arcs, with an emphasis on primitive andesite and lower crust. *The Crust*, *3*, 593–659.

Kelemen, P., Rilling, J. L., Parmentier, E. M., Mehl, L., & Hacker, B. R. (2003). Thermal structure due to solid-state flow in the mantle wedge beneath arcs. In J. Eiler (Ed.), *Inside the Subduction Factory* (pp. 293–311). Washington, DC: American Geophysical Union.

Keller, T., & Katz, R. (2016). The role of volatiles in reactive melt transport in the asthenosphere. *Journal of Petrology*, *57*, 1073–1108.

Liu, Y., He, D., Gao, C., Foley, S., Gao, S., Hu, Z., et al. (2015). First direct evidence of sedimentary carbonate recycling in subduction-related xenoliths. *Nature Scientific Reports*, *5*, 11547. https://doi.org/10.1038/srep11547

Mann, U., & Schmidt, M. (2015). Melting of pelitic sediments at subarc depths: 1. Flux vs. fluid-absent melting and a parameterization of melt productivity. *Chemical Geology*, *404*, 150–167.

Marschall, H. R., & Schumacher, J. C. (2012). Arc magmas sourced from mélange diapirs in subduction zones. *Nature Geoscience*, *5*(12), 862–867.

Marsh, B. (1979). Island arc development: Some observations, experiments, and speculations. *The Journal of Geology*, *87*, 687–713.

Marsh, B. D., & Carmichael, I. S. E. (1974). Benioff zone magmatism. *Journal of Geophysical Research*, *79*(8), 1196–1206. https://doi.org/10.1029/JB079i008p01196

McKenzie, D. (1969). Speculations on the consequences and causes of plate motions. *Geophysical Journal International*. https://doi.org/10.1111/j.1365-246X.1969.tb00259.x

McKenzie, D. (1984). The generation and compaction of partially molten rock. *Journal of Petrology*, *25*, 713–765.

Miller, K. J., Zhu, W.-l., Montesi, L., & Gaetani, G. (2014). Experimental quantification of permeability of partially molten mantle rock. *Earth and Planetary Science Letters*, *388*, 273–282.

Miller, N. C., & Behn, M. D. (2012). Timescales for the growth of sediment diapirs in subduction zones. *Geophysical Journal International*, *190*, 1361–1377. https://doi.org/10.1111/j.1365-246X.2012.05565.x

Nielsen, S. G., & Marschall, H. R. (2017). Geochemical evidence for mélange melting in global arcs. *Science Advances*, *3*(4), e1602402. https://doi.org/10.1126/sciadv.1602402

Phipps, M. J. (1987). Melt migration beneath mid-ocean spreading centers. *Geophysical Research Letters*, *14*, 1238–1241.

Plank, T., & Langmuir, C. H. (1993). Tracing trace elements from sediment input to volcanic output at subduction zones. *Nature*, *362*, 739–743.

Richter, F., & McKenzie, D. (1984). Dynamical models for melt segregation from a deformable matrix. *Journal of Geology*, *92*, 729–740.

Riley, G., & Kohlstedt, D. (1991). Kinetics of melt migration in upper mantle-type rocks. *Earth and Planetary Science Letters*, *105*, 500–521.

Schiemenz, A., Liang, Y., & Parmentier, M. (2011). A high-order numerical study of reactive dissolution in an upwelling heterogeneous mantle—I. Channelization, channel lithology and channel geometry. *Geophysical Journal International*, *186*, 641–664.

Schmeling, H. (2000). Partial melting and melt segregation in a convecting mantle, Physics and Chemistry of Partially Molten Rocks, Volume 11 of the series. *Petrology and Structural Geology*, 141–178. https://doi.org/10.1007/978-94-011-4016-4_5

Schmeling, H., Cruden, A., & Marquart, G. (1988). Finite deformation in and around a fluid sphere moving through a viscous medium: Implications for diapiric ascent. *Tectonophysics*, *149*, 17–34.

Schmeling, H., Marquart, G., Weinberg, R., & Wallner, H. (2019). Modelling melting and melt segregation by two-phase flow: New insights into the dynamics of magmatic systems in the continental crust. *Geophysical Journal International*, *217*, 422–450.
Schmeling, H., & Wallner, H. (2012). Magmatic lithospheric heating and weakening during continental rifting: A simple scaling law, a 2-D thermomechanical rifting model and the East African Rift System. *Geochemistry, Geophysics, Geosystems*, *13*, Q08001. https://doi.org/10.1029/2012GC004178
Schmidt, M. W. (2015). Melting of Pelitic sediments at subarc depths: 2. Melt Chemistry and a parameterization of melt composition. *Chemical Geology*, *404*, 168–182. https://doi.org/10.1016/j.chemgeo.2015.02.013
Scott, D. R., & Stevenson, D. (1984). Magma solitons. *Geophysical Research Letters*, *11*, 1161–1164.
Scott, D. R., & Stevenson, D. (1986). Magma ascent by porous flow. *Journal of Geophysical Research*, *91*, 9283–9296.
Sleep, N. (1984). Tapping of magmas from ubiquitous mantle heterogeneities. *Journal of Geophysical Research*, *89*(B12), 10,029–10,041. https://doi.org/10.1029/JB089iB12p10029
Spencer, C., Cavosie, A. J., Raub, T. D., Rollinson, H., Jeon, H., Searle, M. P., et al. (2017). Evidence for melting mud in Earth's mantle from extreme oxygen isotope signatures in zircon. *Geology*, *45*, 975–978.
Spiegelman, M. (1993). Flow in deformable porous media. part 1. Simple analysis. *Journal of Fluid Mechanics*, *247*, 17–38.
Spiegelman M., Katz, R., & Simpson G., (2007). An introduction and tutorial to the "McKenzie Equations" for magma migration. Retrieved from https://wiki.geodynamics.org/_media/wg:magma_migration:benchmark:1_katz_2007.pdf
Tirupathi, S., Hesthaven, J. S., & Liang, Y. (2014). Modeling 3D magma dynamics using a discontinuous Galerkin Method. *Communications in Computational Physics. Retrieved from* https://infoscience.epfl.ch/record/197481.
van Keken, P., Currie, C., King, S., Behn, M. D., Cagnioncle, A., He, J., et al. (2008). A community benchmark for subduction zone modeling. *Physics of the Earth and Planetary Interiors*, *171*(1-4), 187–197. https://doi.org/10.1016/j.pepi.2008.04.015
von Bargen, N., & Waff, H. (1986). Permeabilities, interfacial areas and curvatures of partially molten systems: Results of numerical computations of equilibrium microstructures. *Journal of Geophysical Research*, *91*(B9), 9261–9276. https://doi.org/10.1029/JB091iB09p09261
von Huene, R., & Scholl, D. (1991). Observations at convergent margins concerning sediment subduction, subduction erosion, and the growth of continental crust. *Reviews of Geophysics*, *29*(3), 279–316.
Wada, I., Behn, M. D., & He, J. (2011). Grain size distribution in the mantle wedge of subduction zones. *Journal of Geophysical Research*, *116*, B10203. https://doi.org/10.1029/2011JB008294
Wada, I., & Wang, K. (2009). Common depth of slab-mantle decoupling: Reconciling diversity and uniformity of subduction zones. *Geochemistry, Geophysics, Geosystems*, *10*, Q10009. https://doi.org/10.1029/2009GC002570
Wark, D. A., & Watson, E. B. (1998). Grain-scale permeabilities of texturally equilibrated, monomineralic rocks. *Earth and Planetary Science Letters*, *164*, 591–605.
Wark, D. A., Williams, C. A., Watson, E. B., & Price, J. (2003). Reassessment of pore shapes in microstructurally equilibrated rocks, with implications for permeability of the upper mantle. *Journal of Geophysical Research*, *108*. https://doi.org/10.1029/2001JB001575
Zhu, G., Gerya, T. V., Yuen, D. A., Honda, S., Yoshida, T., & Connolly, J. A. D. (2009). Three-dimensional dynamics of hydrous thermal-chemical plumes in oceanic subduction zones. *Geochemistry, Geophysics, Geosystems*, *10*, Q11006. https://doi.org/10.1029/2009GC002625
Zhu, W., Gaetani, G. A., Fusseis, F., Montesi, L., & De Carlo, F. (2011). Microtomography of partially molten rocks: Three-dimensional melt distribution in mantle peridotite. *Science*, *332*(6025), 88–91.
Zhu, W., & Hirth, G. (2003). A network model for permeability in partially molten rocks. *Earth and Planetary Science Letters*, *212*(3-4), 407–416. https://doi.org/10.1016/S0012-821X(03)00264-4